

Northumbria Research Link

Citation: Emran, Mohammed Y., Shenashen, Mohamed A., Elmarakbi, Ahmed, Selim, Mahmoud M. and El-Safty, Sherif A. (2022) Hierarchical engineering of Mn₂O₃/carbon nanostructured electrodes for sensitive screening of acetylcholine in biological samples. *New Journal of Chemistry*, 46 (32). pp. 15557-15566. ISSN 1144-0546

Published by: Royal Society of Chemistry

URL: <https://doi.org/10.1039/d2nj02390c> <<https://doi.org/10.1039/d2nj02390c>>

This version was downloaded from Northumbria Research Link: <https://nrl.northumbria.ac.uk/id/eprint/49792/>

Northumbria University has developed Northumbria Research Link (NRL) to enable users to access the University's research output. Copyright © and moral rights for items on NRL are retained by the individual author(s) and/or other copyright owners. Single copies of full items can be reproduced, displayed or performed, and given to third parties in any format or medium for personal research or study, educational, or not-for-profit purposes without prior permission or charge, provided the authors, title and full bibliographic details are given, as well as a hyperlink and/or URL to the original metadata page. The content must not be changed in any way. Full items must not be sold commercially in any format or medium without formal permission of the copyright holder. The full policy is available online: <http://nrl.northumbria.ac.uk/policies.html>

This document may differ from the final, published version of the research and has been made available online in accordance with publisher policies. To read and/or cite from the published version of the research, please visit the publisher's website (a subscription may be required.)

ARTICLE

Hierarchical Engineering of Mn₂O₃/Carbon Nanostructured Electrodes for Sensitive Screening of Acetylcholine in Biological Sample

Received 00th January 20xx,
Accepted 00th January 20xx

M. Y. Emran^{a,b}, M. A. Shenashen^{a,c}, A. Elmarakbi^d, M. M. Selim^e, S. A. El-Safty^{a,*}

DOI: 10.1039/x0xx00000x

Enzymeless electrochemical sensors have received considerable interest for the direct, sensitive, and selective monitoring of biomolecules in a complex biological environment. Here, we designed a nonenzymatic electrochemical sensor based on Mn₂O₃ nanolayers (NLs)/carbon (C) and Mn₂O₃ flower-like (FL)/C structure to detect acetylcholine (ACh) molecules in human fluids. The sensing property and electrochemical activity varied based on the structural and chemical composition of Mn₂O₃-based materials. The Mn₂O₃NLs/C structure of two-dimensional NLs was arranged in parallel with a heterogeneous surface texture, stair-like step-by-step layer formation, and cracked layers that formed free spaces. The Mn₂O₃FL/C were formed with an FL structure. The parallel and perpendicular buildup of sheets from the bottom to top and sheets spreading in all directions formed the FL structure of Mn₂O₃ with multi-structural defects and edges, and heterogeneous surface texture. This unique surface property of Mn₂O₃FL/C and composition facilitated the target diffusion through the inner/outer surface and shortened the distance pathway. Moreover, the Carbon presence on the surface of Mn₂O₃ induced the sensitivity and stability of Mn₂O₃, enhanced the electrochemical activity with high catalytic activity, hastened the electron diffusion, and high loading of ACh molecules. The nonenzymatic ACh sensors of Mn₂O₃NLs/C and Mn₂O₃FL/C showed a good sensor design with low limits of detection (2 and 7 μM, respectively) and a linear range of 0.1–7 mM. The fabricated sensors provided high stability and selectivity, easy fabrication, multi-usage, and fast response motioning of ACh in a complex mixture of human fluids. The designed nonenzymatic sensors of Mn₂O₃NLs/C and Mn₂O₃FL/C signaled the ACh molecules with high stability and selectivity and can be used to investigate and follow up on several neuronal disorders.

Introduction

Neurotransmitters are various kinds of molecules and proteins that are founded in the central nervous systems and are responsible for signal transduction [5, 6]. Choline (Ch) and acetylcholine (ACh) are neurotransmitter molecules that play a key role in signaling transduction and central nervous system functionality. In the central nervous system, these molecule levels are regarded as an indicator for various neuronal diseases¹⁻⁴. Therefore, the controlled detection of ACh in human solutions and the brain is highly required. Various neuronal diseases (i.e., Alzheimer's disease, Parkinson's disease, Huntington's disease dystonia, and multiple sclerosis) could be

investigated and followed up upon recognizing the Ch and ACh levels¹⁻⁴. These diseases are associated with age as the largest risk factor. The control measures and follow-up of these diseases are related to the screening of neurotransmitters in human fluids, the brain, and the central nervous system. The ACh chemical structure lacks an active center of electroactive redox groups, chromophore, or fluorophore groups⁷. So, the Faradaic electron transfer-based method isn't suitable for ACh detection. Thus, the enzyme-based biosensors have been employed for ACh detection by immobilizing Ch and ACh esterase at the active electrode surface⁸⁻¹⁰. The direct detection of ACh with a simple method and enzymeless-based biosensor has attained great interest and development progress to produce highly efficient ACh sensors.

Various analytical methods have been applied for qualitative and quantitative investigation of ACh molecules in biological samples. Various techniques, such as photoluminescence¹⁶, electrochemiluminescence¹¹⁻¹⁴, mass spectrometry¹⁷, ion-sensitive field-effect transistors¹⁸, colorimetry¹⁵, and electrochemical methods^{7, 9, 19, 20} have been implemented to detect the ACh levels. Although most of these techniques show good sensitivity and selectivity in the assays for ACh detection, they suffer from many limitations including complex processes, highly expensive machines, long time detection, lack of portable fabrication, and complicated self-using device. In this context, the electrochemical technique shows proper features such as easy fabrication, simple analysis

^a National Institute for Materials Science (NIMS), Research Center for Functional Materials, 1-2-1 Sengen, Tsukuba-shi, Ibaraki-ken 305-0047, Japan.

^b Chemistry Department, Faculty of Science, Al-Azhar University, Assiut 71524, Egypt

^c Department of Petrochemical, Egyptian Petroleum Research Institute (EPRI), Cairo 11727, Egypt

^d Faculty of Engineering and Environment, Northumbria University, Newcastle upon Tyne, NE1 8ST, UK.

^e Al-Aflaj College of Science and Human Studies, Prince Sattam Bin Abdulaziz University, Al-Aflaj, 710-11912, Saudi Arabia.

*Correspondence: sherif.elsafty@nims.go.jp

Homepage: https://samurai.nims.go.jp/profiles/sherif_elsafty

Electronic Supplementary Information (ESI) available: [1- Experimental section of Materials, Electrochemical detection of ACh on Mn₂O₃NLs/C/GCE and Mn₂O₃FL/C/GCE, Characterization analyses; 2- Results and discussions of electrode surface area; Figure S1; Figure S2; Figure S3; Table S1]. See DOI: 10.1039/x0xx00000x

without further purification, portable design, disposable use, and high economic value for ACh detection²¹⁻²³. Therefore, electrochemical techniques offer definitive analytical strategies for quantifying ACh in various resources and receptors with good sensitivity and selectivity.

Engineering and modification of working electrodes using the synthesis of electroactive materials such as graphene, multi-walled carbon nanotubes (MWCNTs), metal nanoparticles, metal oxides (MOs), and others are key factors for the development of electrochemical sensors^{10, 15, 18, 24-28}. MOs and their composites have been widely used in various electrochemical applications of batteries, supercapacitors, and sensors²⁸⁻³⁴. Among transition metal oxides, manganese (III) oxide (Mn_2O_3) has gained great interest due to various factors, such as its easy synthesis and fabrication, high stability, and good electrochemical and optical properties³⁴⁻³⁹. Mn oxide materials have been widely used as electroactive materials for detecting various targets (i.e., H_2O_2 , glucose (GI), DA, and glutathione^{35, 36, 38, 40, 41}). Various morphological structures and composites of MnO_2 -based materials such as $\text{MnO}_2/\text{F-MWCNT}/\text{Ta}$ ⁴², $\text{MnO}_2/\text{CNT}/\text{Ta}$ ⁴³, MnO_2 nanostructures/ Ta ⁴⁴, MnO_2 nanosheets⁴⁵, $\text{Au}/\text{MnO}_2/\text{GR-CNTs}$ ⁴⁶, ZnO/MnO_2 ³⁸, porous CNT/MnO_2 ⁴⁰, and $\text{Au}/\text{MnO}_2\text{-gC}_3\text{N}_4/\text{TiO}_2$ have been used for sensing and biosensing applications including the detection of H_2O_2 , DA, GI, and lactose. MOs in sensing and biosensing applications suffer from a lack of sensitivity, durability, and stability^{47, 48}. Various composite materials of MOs and carbon-based materials (i.e., graphene, CNTs, MWCNS, carbon fibers, and carbon dots (CDs)) have been used to sustain electrochemical and optical properties^{27, 28, 34, 40-43, 48, 49}. Therefore, controlling the synthesis of MOs and carbon-based materials to produce novel composite materials with high optical and electrochemical properties is of great interest.

Herein, a novel material consisting of two structures of Mn_2O_3 nanolayers (NLs)/carbon (C) and Mn_2O_3 flower-like (FL)/C $\text{Mn}_2\text{O}_3/\text{C}$ ($\text{Mn}_2\text{O}_3\text{NLs}/\text{C}$ and $\text{Mn}_2\text{O}_3\text{FL}/\text{C}$, respectively) were designed. The materials were synthesized using a simultaneous and simple approach (hydrothermal treatment (HT)). The starting materials influenced the construction of Mn_2O_3 , where GI acted as the reducing agent and directing agent of $\text{Mn}_2\text{O}_3\text{NLs}/\text{C}$. The creation of $\text{Mn}_2\text{O}_3\text{FL}/\text{C}$ was controlled by using sodium citrate as the directing agent. The prepared $\text{Mn}_2\text{O}_3\text{NLs}/\text{C}$ and $\text{Mn}_2\text{O}_3\text{FL}/\text{C}$ were used for direct electrochemical signaling of ACh (nonenzymatic sensor). The $\text{Mn}_2\text{O}_3\text{FL}/\text{C}$ exhibited a structural morphology of parallel stair-like stacked NLs with a free space in between, heterogeneous outer surface morphology, rough surface, and multiple edges. The controlled structure of $\text{Mn}_2\text{O}_3\text{FL}/\text{C}$ advanced the electrochemical catalytic functionality and sensing property. The centrally spreading Mn_2O_3 sheets formed the $\text{Mn}_2\text{O}_3\text{FL}/\text{C}$ structure in parallel and perpendicularly to form a micrometric FL structure. The $\text{Mn}_2\text{O}_3\text{FL}/\text{C}$ and $\text{Mn}_2\text{O}_3\text{NLs}/\text{C}$ acted as transducing elements and electrocatalytic mediators for the signaling of ACh molecules. The $\text{Mn}_2\text{O}_3\text{FL}/\text{C}$ sensor showed a better electrochemical performance and higher stable and sensitive nonenzymatic ACh-sensing property than the $\text{Mn}_2\text{O}_3\text{NLs}/\text{C}$ sensor. These sensors provided high sensitivity and selectivity, opening possibilities for application in monitoring of ACh in biological samples (i.e., human serum samples). Therefore, the designed

nonenzymatic ACh sensors can be used for clinical investigations of several neuronal diseases.

Experimental

$\text{Mn}_2\text{O}_3\text{NLs}$ and FL structures synthesis

Control of the synthesis of $\text{Mn}_2\text{O}_3\text{NLs}/\text{C}$ and $\text{Mn}_2\text{O}_3\text{FL}/\text{C}$ structures was achieved via a one-pot HT approach. The $\text{Mn}_2\text{O}_3\text{NLs}/\text{C}$ material was prepared as follows: The KMnO_4 acts as the Mn_2O_3 source and the ascorbic acid (AA) solution acts as the carbon source, reducing and directing agent. 0.2 g of KMnO_4 (0.02 M) was added to 30 mL deionized H_2O (DI H_2O) with continuous stirring for 1 h (KMnO_4 solution). 1.4 g of AA (0.13 M) was dissolved in 30 mL DI H_2O (AA solution). The AA and KMnO_4 solutions were mixed and then continuously stirred for 2 h, then this mixture solution was treated hydrothermally at 180 °C for 6 h. Similarly, the $\text{Mn}_2\text{O}_3\text{FL}/\text{C}$ were synthesized using the same procedures described earlier. The AA solution contained 1.4 g AA + 1.4 g Na citrate was dissolved in 30 mL DI- H_2O . The AA was added to KMnO_4 solution gently under stirring. Then, the formed mixture was treated hydrothermally at 180 °C for 6 h.

After cooling, a reddish precipitate was collected and washed many times using water/ethanol (1:1) to eliminate unwanted and unreacted molecules. The collected materials were dried in an oven at 60 °C for 24 h. The materials were annealed at 600 °C for 4 h under N_2 flow. The materials, named Mn_2O_3 NLs/C and Mn_2O_3 FL/C were collected and stored in an isolated environment for use in the sensor design.

Electrode design of $\text{Mn}_2\text{O}_3\text{NLs}/\text{C}/\text{GCE}$ and $\text{Mn}_2\text{O}_3\text{FL}/\text{C}/\text{GCE}$

The modified electrodes of $\text{Mn}_2\text{O}_3\text{NLs}/\text{C}/\text{GCE}$ and $\text{Mn}_2\text{O}_3\text{FL}/\text{C}/\text{GCE}$ were assembled based on ink formation, drop-casting, and drying. Step 1, preparation of $\text{Mn}_2\text{O}_3\text{NLs}/\text{C}/\text{GCE}$ and $\text{Mn}_2\text{O}_3\text{FL}/\text{C}/\text{GCE}$ ink solutions were formed by dispersing separately 10 mg of each material ($\text{Mn}_2\text{O}_3\text{NLs}/\text{C}/\text{GCE}$ and $\text{Mn}_2\text{O}_3\text{FL}/\text{C}/\text{GCE}$) in 1 mL DI- H_2O (sonicated for 1 h). Step 2, electrode pre-treatment and fabrication, the GCEs were polished using alumina (1%) and diamond (0.05 %) slurries several times to attain a mirror-like surface. Step 3, 10 μL of each $\text{Mn}_2\text{O}_3\text{NLs}/\text{C}$ and $\text{Mn}_2\text{O}_3\text{FL}/\text{C}$ ink solution was dropped on the GCE surface and then kept dried at 25 °C. The fabricated GCEs of $\text{Mn}_2\text{O}_3\text{NLs}/\text{C}/\text{GCE}$ and $\text{Mn}_2\text{O}_3\text{FL}/\text{C}/\text{GCE}$ were activated and stabilized using the cyclic voltammetry (CV) technique in 0.1 M NaOH (scan rate of 100 mVs^{-1} and applied potential scanning of -0.6 V to +1.6 V).

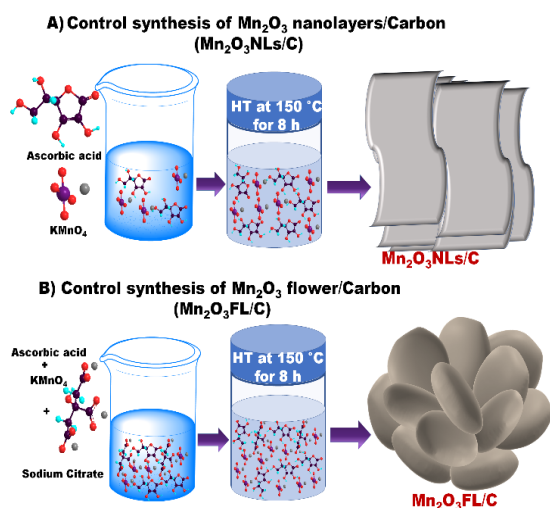
Actual monitoring of ACh using nonenzymatic sensors of $\text{Mn}_2\text{O}_3\text{NLs}/\text{C}/\text{GCE}$ and $\text{Mn}_2\text{O}_3\text{FL}/\text{C}/\text{GCE}$

The ACh levels in human blood samples and the validity of the designed electrodes for actual monitoring of ACh in complex mixtures (human blood serum samples) were determined using $\text{Mn}_2\text{O}_3\text{NLs}/\text{C}/\text{GCE}$ and $\text{Mn}_2\text{O}_3\text{FL}/\text{C}/\text{GCE}$. The human blood serum solution was set by mixing 100 μL blood serum with 9.9 mL 0.1 M NaOH solution. Standard concentrations of ACh were injected into the human blood solution and measured by the designed electrodes using the chronoamperometry technique (CA). The ACh concentrations in human serum blood samples were measured using CA under $E = 0.6$ V under N_2 saturation at room temperature and continuous stirring.

Results and discussion

Synthesis of $\text{Mn}_2\text{O}_3\text{NLS/C}$ and $\text{Mn}_2\text{O}_3\text{FL/C}$

The synthesis of various nanostructures of Mn_2O_3 was approached using the green synthesis method (HT) (Scheme 1). The oxidation-reduction process occurred under the controlled HT of AA and KMnO_4 . At a high temperature of 180 °C, the AA molecules acted as reducing agents, whereas the KMnO_4 molecules acted as the oxidizing agent. AA was oxidized, and the Mn (VII) ions were reduced to Mn (III) ions. For the formation of $\text{Mn}_2\text{O}_3\text{NLS/C}$, the AA molecules act as the reducing and directing agent to form two-dimensional layers with a cracked and multilayer morphology. After forming the Mn_2O_3 materials, the residual molecules of AA formed the carbon-based materials⁵⁰. Thus, AA acted as the directing agent, reducing agent, and C-source. Similarly, the addition of Na-citrate to the solution of AA and KMnO_4 controlled the formation of the new FL structure of $\text{Mn}_2\text{O}_3\text{FL/C}$ with horizontal and perpendicular sheet arrangements. The Na-citrate with multi-oxygenated groups helped in the orientation and formation of the FL structure due to its branched molecular structure. In addition, citrate acted as the source of C formation within AA. These results were also configured from the energy-dispersive X-ray spectroscopy (XPS) and energy dispersive X-ray-scanning electron microscopy (EDX-SEM). The results showed that the carbon contents of $\text{Mn}_2\text{O}_3\text{FL/C}$ were higher than those of $\text{Mn}_2\text{O}_3\text{NLS/C}$. Therefore, the one-pot synthesis of nanostructured Mn_2O_3 was achieved with a simple approach and without any capping agents. The structural morphology and composition of NLS and FL played key roles in the sensing sensitivity and stability of the prepared materials. **The oxidation of ACh molecules has occurred at Mn_2O_3 surface structures due to their direct contact with Mn atoms and carbon that induced the surface charge and maintained the catalytic stability.**



Scheme 1. The schematic synthesis of Mn_2O_3 structures of nanolayers (A) and flower (B) like structures decorated by carbon.

Surface morphology, composition, and intrinsic properties of $\text{Mn}_2\text{O}_3\text{NLS/C}$ and $\text{Mn}_2\text{O}_3\text{FL/C}$

The composition and surface nature of the prepared materials were investigated using various techniques, including field emission SEM (FE-SEM), X-ray diffraction (XRD), Raman shift, and XPS. The surface

morphology of $\text{Mn}_2\text{O}_3\text{NLS/C}$ was composed of stacked and parallel NLS (Figure 1A). The NLS were stacked and deposited one by one with surface heterogeneity and various free spaces (Figure 1Aa). The free spaces were formed between layers and on the top layer surface, leading to a heterogeneous surface with multi-surface defects of cracked NLS (Figure 1Ab). A rough surface texture was obtained, which possibly appeared as the presence of C at the external surface of $\text{Mn}_2\text{O}_3\text{NLS}$. The parallel and perpendicular axial orientation of NLS formed the surface structure of $\text{Mn}_2\text{O}_3\text{NLS/C}$ with a rough surface texture, multi-free space, outer surface coverage by C, and cracked-like deposited layers. Figures 1B (a–c) show the EDX-SEM mapping of $\text{Mn}_2\text{O}_3\text{NLS/C}$. The EDX-SEM mapping indicated the homogeneous distribution of Mn, C, and O atoms with 59.51, 36.25, and 4.24 %wt, respectively. The EDX mapping confirmed the presence of carbon atoms in the chemical composition of $\text{Mn}_2\text{O}_3\text{NLS}$. Figures 2A (a–d) show the FE-SEM of $\text{Mn}_2\text{O}_3\text{FL/C}$. The layer-by-layer formation of the micrometric FL structure was observed. The focused top-view illustrates the FL construction with an open leaf-like structure and connecting sheets on the centers that spread out in three directions (Figure 2Ab). The side-view-focused image shows the spread of sheets in various directions, merging at the center to form the FL structure (Figure 2Ad). Moreover, the bright dots on the outer surface illustrate the formation of C. In addition, the rough surface texture and bright circular centers established the existence of C at the external surface of $\text{Mn}_2\text{O}_3\text{FL}$ structure. The EDX-SEM mapping of $\text{Mn}_2\text{O}_3\text{FL/C}$ shows a homogeneous existence of Mn-, O-, and C-atoms and confirms the presence of carbon. Mn, O, and C had %wt distributions of 65.09%, 25.56%, and 9.35%, respectively (Figure S1A). These data illustrate the controlled synthesis of various structures of Mn_2O_3 by controlling the starting materials. The FL and stacked NLS of Mn_2O_3 decorated by C on its outer surface can control the surface activity toward the electrooxidation of ACh with facile diffusion of molecules and electrons through the outer/inner surface.

The crystalline structure, crystallinity degree, and Mn_2O_3 formation were illustrated using XRD analysis. Figure 1C shows the XRD patterns of $\text{Mn}_2\text{O}_3\text{NLS/C}$ (a) and $\text{Mn}_2\text{O}_3\text{FL/C}$ (b). The XRD peaks centered at 2θ of 28.75°, 41.92°, and 53.54° corresponded to the 002, 001, and 004 crystal planes of graphite, respectively, indicating the presence of carbon materials in the structure of Mn_2O_3 and ascertaining the formation of C^{22-24, 34}. The formation of $\alpha\text{-Mn}_2\text{O}_3$ was verified from the XRD diffraction peaks with the dominant 222 crystal plane and orthorhombic crystal system (pbca (61))⁵¹. The XRD peaks were centered at 2θ of 23.24°, 33.11°, 38.39°, 45.32°, 49.51°, 55.34°, and 65.95°, which were corresponded to the (211), (222), (400), (332), (431), (440), and (622) planes, respectively ((JCPDS card 151-4104). These data illustrate the highly crystalline degree and purity of $\alpha\text{-Mn}_2\text{O}_3$ decorated by C.

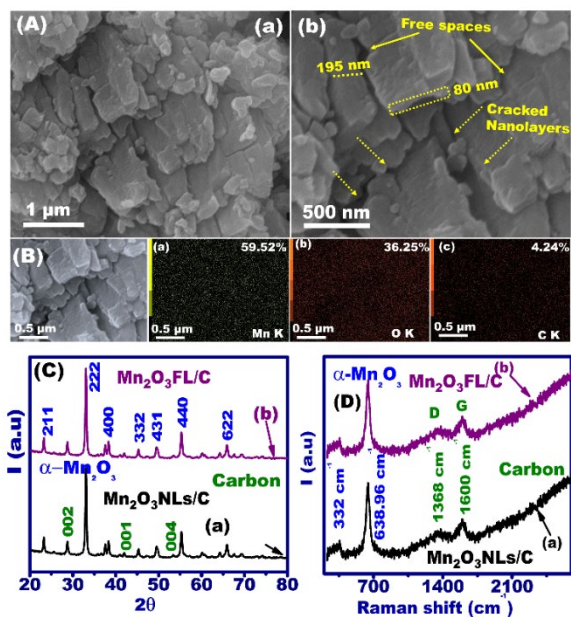


Figure 1. A) The FE-SEM of $\text{Mn}_2\text{O}_3\text{NLS}/\text{C}$ (a) and focused image (b) illustrate the free spaces and cracked nanolayers. B) The EDX-SEM mapping of $\text{Mn}_2\text{O}_3\text{NLS}$ for Mn (a), O (b), and C (c). C[a-d]). C) The WAXRD patterns of $\text{Mn}_2\text{O}_3\text{NLS}/\text{C}$ (a) and $\text{Mn}_2\text{O}_3\text{FL}/\text{C}$ (b). D) The Raman shift spectra of $\text{Mn}_2\text{O}_3\text{NLS}/\text{C}$ (a) and $\text{Mn}_2\text{O}_3\text{FL}/\text{C}$ (b).

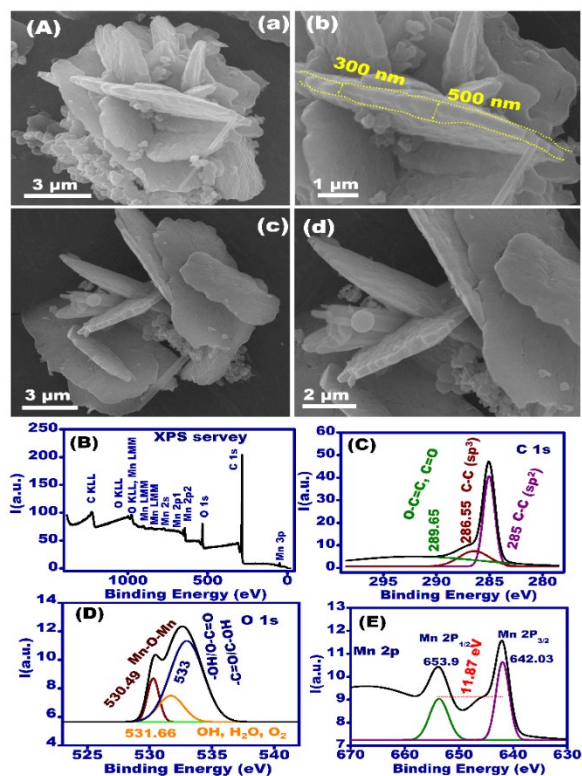


Figure 2. A) The FE-SEM of $\text{Mn}_2\text{O}_3\text{FL}/\text{C}$ at various magnifications and positions (a-d). B) The XPS survey of $\text{Mn}_2\text{O}_3\text{FL}/\text{C}$. The XPS survey of C 1s (C), O 1s (D), and Mn 2p (E).

The Raman spectra of $\text{Mn}_2\text{O}_3\text{NLS}/\text{C}$ (a) and $\text{Mn}_2\text{O}_3\text{FL}/\text{C}$ (b) are presented in Figure 1D. The main peaks of Mn_2O_3 were observed and centered at 332 and 638.96 cm^{-1} . The peaks centered at 1368 and

1600 cm^{-1} are related to the D and G bands, respectively. Therefore, the designed materials were composed of Mn_2O_3 decorated by graphitic carbon in the form of C^{51, 52}. Fourier-transform infrared spectroscopy (FT-IR) showed the formation of Mn_2O_3 , where two broad stretching bands centered at 3452, 1720, and 1612 cm^{-1} were related to the presence of adsorbed H_2O and OH group, C=O, and C=C, respectively (Figure S1E). The FT-IR peaks at 458.86 and 527.79 cm^{-1} were related to the vibrational bending mode of M-O. Therefore, the prepared materials contained Mn_2O_3 and carbon^{53, 54}. The XPS outlines the chemical composition and oxidation states of Mn_2O_3 . Figure 2B shows the XPS of $\text{Mn}_2\text{O}_3\text{FL}/\text{C}$, four main peaks centered at 653.9, 642.03, 530.81, and 284.03 eV are related to Mn 2p_{1/2}, Mn 2p_{3/2}, O 1s, and C 1s, respectively. The two peaks that center at 653.9 and 642.03 are related to the oxidation states of Mn³⁺ (Mn 2p_{1/2}, Mn 2p_{3/2}) with spin-orbit energy separation of 11.87 eV (Figure 2E). These data provide the formation of Mn_2O_3 ⁵⁵⁻⁵⁷. The O 1s XPS survey indicates a broad peak at 532.98 eV, and two peaks at 531.66 and 530.49 eV for various carbon-oxygen groups, adsorbed water (OH, H₂O, and O₂), and Mn-O-Mn, respectively (Figure 2D). Figure 2C shows the C 1s XPS survey and indicates the presence of carbon formation of C-C (sp²), C-C (sp³), and groups of C-O bonds that centered at 285, 286.55, and 289.65 eV, respectively. These results prove the chemical composition of $\text{Mn}_2\text{O}_3\text{NLS}/\text{C}$ and $\text{Mn}_2\text{O}_3\text{FL}/\text{C}$ with high crystalline degrees and C covering the layers and FL structures.

Electrochemical behavior of $\text{Mn}_2\text{O}_3\text{NLS}/\text{C}$ and $\text{Mn}_2\text{O}_3\text{FL}/\text{C}$

The $\text{Mn}_2\text{O}_3\text{NLS}/\text{C}$ and $\text{Mn}_2\text{O}_3\text{FL}/\text{C}$ electrochemical activities were outlined by measuring the behavior of $[\text{Fe}(\text{CN})_6]^{3-/4-}$ in 0.1 M KCl using CV- and EIS- techniques. The electrochemical properties (i.e., catalytic activity and charge transport velocity) of GCE and $\text{Mn}_2\text{O}_3\text{NLS}/\text{C}$ and $\text{Mn}_2\text{O}_3\text{FL}/\text{C}$ were investigated based on the redox peaks' positions (E/V) and the current values (I/ μA) of $\text{Fe}^{3+/2+}$. Figure S2A shows the CV measurements of $\text{Mn}_2\text{O}_3\text{NLS}/\text{C}$ (blue line), $\text{Mn}_2\text{O}_3\text{FL}/\text{C}$ (red line), and GCE (black line). The $\text{Mn}_2\text{O}_3\text{FL}/\text{C}/\text{GCE}$ exhibited a high I_a value (22.45 μA) and low peak-to-peak separation potential values ($\Delta E = 0.171$ V) compared to the $\text{Mn}_2\text{O}_3\text{NLS}/\text{C}$ ($I_a = 15.6$ μA , $\Delta E = 0.202$ V) and GCE ($I_a = 10.4$ μA , $\Delta E = 0.214$ V). Therefore, the $\text{Mn}_2\text{O}_3\text{FL}/\text{C}/\text{GCE}$ showed high electrochemical performance⁵⁹. This result may associate with Mn-atom's presence and activity, the presence of C on the inner/outer surface, the morphological structure of FL, and numerous free spaces interior/exterior of the FL surface. The surface areas of GCE, $\text{Mn}_2\text{O}_3\text{NLS}/\text{C}/\text{GCE}$, and $\text{Mn}_2\text{O}_3\text{FL}/\text{C}/\text{GCE}$ were calculated to be 0.374×10^{-3} , 0.604×10^{-3} , and 2.21×10^{-3} cm^2 , respectively, based on Randles-Sevcik equation⁵⁹ (for more information, see supporting information).

The EIS measurements are one of the tools that are used for outlining the electrochemical properties of the fabricated electrodes^{49, 60-62}. The EIS examination of GCE, $\text{Mn}_2\text{O}_3\text{NLS}/\text{C}/\text{GCE}$, and $\text{Mn}_2\text{O}_3\text{FL}/\text{C}/\text{GCE}$ showed the surface resistance and electron diffusion pathway. Figure S2B displays the -Nyquist plots of GCE (black line) $\text{Mn}_2\text{O}_3\text{NLS}/\text{C}/\text{GCE}$ (blue line), and $\text{Mn}_2\text{O}_3\text{FL}/\text{C}/\text{GCE}$ (red line) in 1 mM $[\text{Fe}(\text{CN})_6]^{3-/4-}$. The inset Figure S2B demonstrates the equivalent circuit of the EIS. The surface charge resistance (R_{ct}) is represented by the semicircle outlines, while the electron diffusion velocity is represented by lines⁶¹⁻⁶⁵. The $\text{Mn}_2\text{O}_3\text{FL}/\text{C}/\text{GCE}$ displayed a low

semicircle and high line pathway. While the GCE and $\text{Mn}_2\text{O}_3\text{NLs/C/GCE}$ showed a high semicircle and low line pathway. Therefore, the $\text{Mn}_2\text{O}_3\text{FL/C/GCE}$ shows high electron diffusion and low surface charge resistance. The electrochemical activity of $\text{Mn}_2\text{O}_3\text{FL/C/GCE}$ may associate with a) the rich Mn atoms in contact and distributed on the outer surface of Mn_2O_3 and b) the FL structure surface morphology with NLs formed by layer buildup, numerous free spaces interior and exterior the materials surface, and the presence of C at the outer surface. The C played a crucial role in enhancing the electron mobility, enriching the negative charge surface, stabilizing, sustaining the catalytic activity, and supporting the multi-functional active surface foundation.

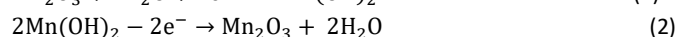
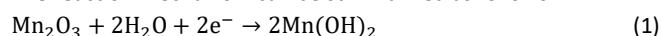
Active signaling of ACh on $\text{Mn}_2\text{O}_3\text{NLs/C}$ and $\text{Mn}_2\text{O}_3\text{FL/C}$

The $\text{Mn}_2\text{O}_3\text{NLs/C/GCE}$ and $\text{Mn}_2\text{O}_3\text{FL/C/GCE}$ sensing functionality for detection of ACh was examined using CV measurements. Figure 3A shows the CV measurements of ACh (1.5 mM) on GCE (black line) and $\text{Mn}_2\text{O}_3\text{NLs/C/GCE}$ (green line). A high CV signal was observed during the ACh electrooxidation on the surface of $\text{Mn}_2\text{O}_3\text{NLs/C/GCE}$, whereas no response was observed on the GCE. This behavior indicates that the $\text{Mn}_2\text{O}_3\text{NLs/C/GCE}$ can detect ACh molecules through a direct electrooxidation process using a Mn_2O_3 -based surface. Figure 3B shows the CVs of 0 (background) and 1.5 mM ACh for $\text{Mn}_2\text{O}_3\text{NLs/C/GCE}$. This behavior confirmed the formation of a highly active catalytic surface, where a broad anodic peak at 0.6 V was detected compared with the background. This anodic peak is related to the ACh electrocatalytic oxidation on the $\text{Mn}_2\text{O}_3\text{NLs/C/GCE}$ surface. Figure 3C shows the ACh (1.5 mM) CVs on the $\text{Mn}_2\text{O}_3\text{FL/C/GCE}$ surface. A broad anodic peak centered at 0.6 V was observed on $\text{Mn}_2\text{O}_3\text{FL/C/GCE}$, whereas no peaks were obtained on the surface of bare GCE. Moreover, the ACh sensing on the $\text{Mn}_2\text{O}_3\text{FL/C/GCE}$ surface was tested using CV of 0 (black ground) and 1.5 mM ACh (Figure 3D). These results indicate the ACh catalytic oxidation on the surface of $\text{Mn}_2\text{O}_3\text{FL/C/GCE}$. Figure 3E shows the CV of 1.5 mM ACh on $\text{Mn}_2\text{O}_3\text{NLs/C/GCE}$ (black line) and $\text{Mn}_2\text{O}_3\text{FL/C/GCE}$ (green line). The $\text{Mn}_2\text{O}_3\text{FL/C/GCE}$ showed a better performance and higher CV anodic peak current than $\text{Mn}_2\text{O}_3\text{NLs/C/GCE}$. This behavior may be related to the structural formation of an FL structure with multi-direction orientation, free spaces, ridges end, rough surface texture, and surface heterogeneity.

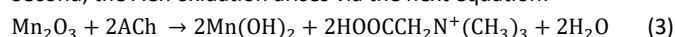
The ACh electrooxidation interaction mechanism on the surface of $\text{Mn}_2\text{O}_3/\text{GCE}$ has been outlined⁶⁶⁻⁶⁸.

First, the anodic and cathodic peaks of Mn_2O_3 are attributed to the redox process of $\text{Mn}^{3+}/\text{Mn}^{2+}$.

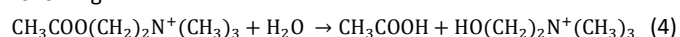
The reaction mechanism can be summarized as follows.



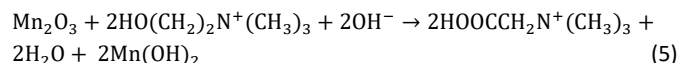
Second, the ACh oxidation arises via the next equation:



Based on the previous works, step 2 outlines the conclusion of the following^{19, 69}:



Then, the hydroxyethyl groups oxidized as follows:



In an alkaline solution, the ACh molecules are hydrolyzed to liberate acetate anions and Choline (Ch) molecules. Mn (III) was reduced to Mn (II). Mn (III) is unstable and reduced easily to Mn (II) with a high capability of oxidizing the biomolecules via the redox reaction mechanism in alkaline solutions under honestly applied potential. The Ch-molecules have been oxidized to carboxylic acid by forming Mn (III)^{67, 68}. The $\text{Mn}_2\text{O}_3\text{FL/C/GCE}$ and $\text{Mn}_2\text{O}_3\text{NL/C/GCE}$ act as the highly efficient surface for ACh-molecules electrooxidation. Therefore, flow and current intensity are related to the concentrations of ACh- molecules during oxidation.

The kinetic mechanism of ACh on $\text{Mn}_2\text{O}_3\text{FL/C/GCE}$ and $\text{Mn}_2\text{O}_3\text{NLs/C/GCE}$ surfaces was explored using CVs at a certain scan function rate. Figure S3A shows the CVs of ACh electrooxidation (1.5 mM) on $\text{Mn}_2\text{O}_3\text{NLs/C/GCE}$ in 0.1 M NaOH under scan rate dependent function (50–300 mVs^{-1}). The I_a (μA) increases as the increase of scan rate. In the plotting function of the square root of scan rate versus I_a (μA)-values, a linear relationship was indicated, and the regression equation was I_a (μA) = $-4.25 + 0.959 v^{0.5}$ (mVs^{-1}), $R^2 = 0.994$ (Figure S3B). Similarly, the scan rate effect on ACh catalytic oxidation (mVs^{-1}) was studied on $\text{Mn}_2\text{O}_3\text{FL/C/GCE}$. Figure S3C shows the CVs of ACh (1.5 mM) under scan rate functionality of 50–300 mVs^{-1} . The I_a (μA) increases as the increase in scan rate values. The relationship between the scan rate (mVs^{-1}) versus the I_a (μA) was linear and the regression equation was I_a (μA) = $-5.62 + 1.3 v^{0.5}$ (mVs^{-1}), $R^2 = 0.995$ (Figure S3D). These data illustrate that the kinetic mechanism of the ACh at the surface of $\text{Mn}_2\text{O}_3\text{NLs/C/GCE}$ and $\text{Mn}_2\text{O}_3\text{FL/C/GCE}$ is a diffusion mechanism^{19, 65-70}.

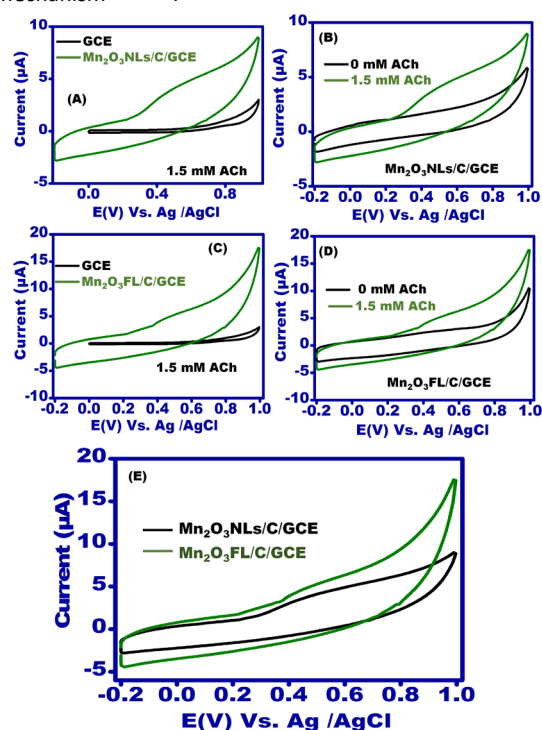


Figure 3. A) The CVs of GCE (black line) and $\text{Mn}_2\text{O}_3\text{NLs/C/GCE}$ (green line) in 0.1 M NaOH containing 1.5 mM ACh. B) The CVs of $\text{Mn}_2\text{O}_3\text{NLs/Cs/GCE}$ in 0.1 M NaOH and 0.1 M NaOH containing 1.5 M

ACh. C) The CVs of GCE (black line) and $\text{Mn}_2\text{O}_3\text{FL/C/GCE}$ (green line) in 0.1 M NaOH containing 1.5 mM ACh. D) The CVs of $\text{Mn}_2\text{O}_3\text{FL/C/GCE}$ in 0.1 M NaOH (black line) and 0.1 M NaOH containing 1.5 M ACh (green line). E) The CVs of $\text{Mn}_2\text{O}_3\text{NLS/C/GCE}$ (black line) and $\text{Mn}_2\text{O}_3\text{FL/C/GCE}$ (green line) in 0.1 M NaOH containing 1.5 mM ACh.

Nonenzymatic sensitive sensor assay for detection of ACh based on $\text{Mn}_2\text{O}_3\text{NLS/C/GCE}$ and $\text{Mn}_2\text{O}_3\text{FL/C/GCE}$

The design of a sensitive and selective sensor for ACh detection is highly required for point-of-care diagnosis. The key points for nonenzymatic sensors are simplicity, direct detection, reusability, and efficient stability. We studied ACh-sensitive detection on various electrodes of $\text{Mn}_2\text{O}_3\text{NLS/C/GCE}$ and $\text{Mn}_2\text{O}_3\text{FL/C/GCE}$ using the chronoamperometry (CA) technique. Figure 4A shows the CA response upon multiple injections of ACh concentrations (0.1–6.5 mM) at an applied potential of 0.6 V under N_2 saturation and continuous stirring on $\text{Mn}_2\text{O}_3\text{FL/C/GCE}$. Sensitive and fast (within 5 s) CA-current response was detected upon the adding of ACh concentrations with stable and gradual current increase (inset of Figure 4A). The calibration curve showed a linear relationship between the $[\text{ACh}]/(\text{mM})$ versus the I_a (μA) (Figure 4B). The regression equation is $I(\mu\text{A}) = 5.56 + 7.87 [\text{ACh}](\text{mM})$, $R^2 = 0.997$. The limit of detection (LOD) was calculated to be 0.002 mM based on $3\sigma/s$ (σ is the standard error of intercept; s is the slope value) for the full range of 0.1–6.5 mM. The stable and linear response at low range of 0.1–1 mM was observed with a LOD of 0.002 mM ($I(\mu\text{A}) = 4.985 + 8.5 [\text{ACh}](\text{mM})$, $R^2 = 0.997$) (Figure 4C). These data illustrate the highly sensitive and stable ACh sensor assay based on $\text{Mn}_2\text{O}_3\text{FL/C/GCE}$. The same response was observed in the detection of ACh concentrations by $\text{Mn}_2\text{O}_3\text{NLS/C/GCE}$ with less sensitivity than $\text{Mn}_2\text{O}_3\text{FL/C/GCE}$ (Figure 4D). A high signaling response with a stable reading out was observed upon the injection of ACh concentrations in the range of 0.1–7 mM. The calibration curve showed a linear relationship ($[\text{ACh}]/\text{mM}$ versus I_a (μA)) in the full concentration range with a regression equation of $I_a(\mu\text{A}) = 15.03 + 8.2 [\text{ACh}](\text{mM})$, $R^2 = 0.996$ and LOD of 0.009 mM (Figure 4E). A linear relationship ($[\text{ACh}]/\text{mM}$ versus I_a (μA)) at a low ACh concentration range of 0.1–1 mM was observed with a LOD of 0.007 mM (Figure 4F). The LOD values were affected by the construction of Mn_2O_3 (layers or FL structure), chemical composition, and ACh concentrations. At high concentrations, the possibility of poisoning the active site is high, thus affecting the sensor detection limit⁶⁷. In addition, the $\text{Mn}_2\text{O}_3\text{FL}$ structural morphology facilitated the diffusion of ACh on the outer/inner surface and increased the mass-to-volume ratio. The higher amounts of C and %wt of Mn contents in $\text{Mn}_2\text{O}_3\text{FL/C}$ than $\text{Mn}_2\text{O}_3\text{NLS/C}$ induced high surface stability and increased the sustainability of catalytic active sites⁷²⁻⁷⁴. The presence of a thin layer of carbon materials at the surface of Mn_2O_3 nanostructures forms a pool of electrons at the outer surface that play a key role in sustaining the catalytic active site centers. In addition, the presence of carbon materials increases the conductivity of the electrode. All these factors provided highly sensitive detection of ACh-molecules based on $\text{Mn}_2\text{O}_3\text{FL/C}$ materials. The ACh levels in the nervous system

(synapse) are about ~2.4 mM, leading to a good response and well fits with our reported data^{19, 69}. Table S1 outlines the comparison between the $\text{Mn}_2\text{O}_3\text{FL/C}$, $\text{Mn}_2\text{O}_3\text{NLS/C}$, and other materials in the functions of linear range and LOD values such as Ni–Al hydroxides (LDH)/ mesoporous carbon, hollow nickel microsphere-carbon microparticles, Cu nanoparticles, Ni–Al LDH decorated CDs, Cu/Cu₂O, lichen-like NiO nanostructure, CuCo₂O₄ nanoplates, and magnetic core-shell. The designed sensors ($\text{Mn}_2\text{O}_3\text{FL/C}$ and $\text{Mn}_2\text{O}_3\text{NLS/C}$) showed a good sensitive assay. In addition, these data provide a wide linear range and a low LOD. In addition, the synthesized materials achieved the outcomes of a cost-effective and simple approach.

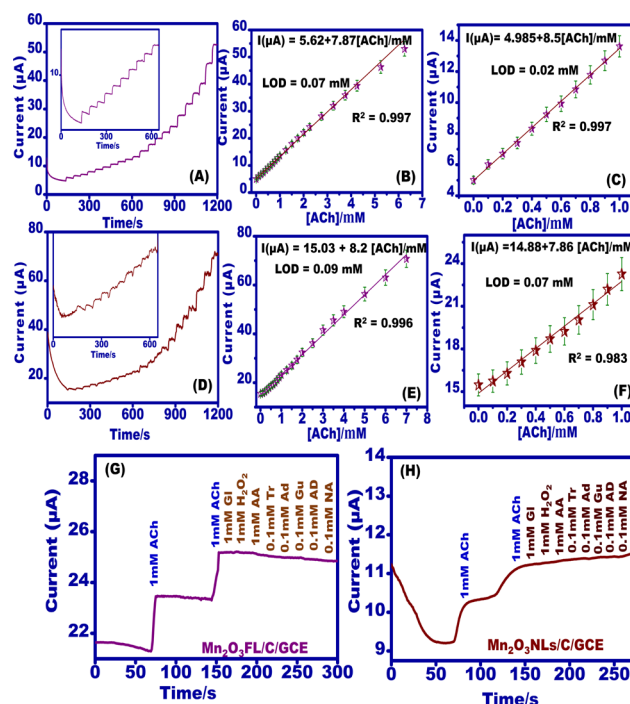


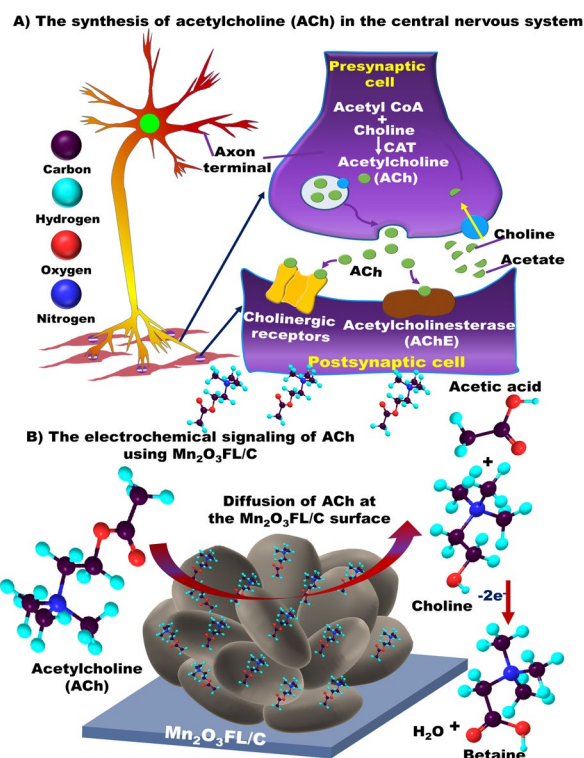
Figure 4. A & its inset) The CA response of ACh concentrations within the range of 0.1–7 mM at $E = 0.6$ V in 0.1 M NaOH solution using $\text{Mn}_2\text{O}_3\text{FL/C/GCE}$. The plot of $[\text{ACh}]/\text{mM}$ Vs the $I_a/\mu\text{A}$ for the range of 0.1–7 mM (B) and low range of 0.1–1 mM (C). D and its inset) The CA response of ACh concentrations (0.1–7 mM) using $\text{Mn}_2\text{O}_3\text{NLS/C/GCE}$. The plot of $[\text{ACh}]/\text{mM}$ Vs $I_a/\mu\text{A}$ for the range of 0.1–7 mM (E) and low range of 0.1–1 mM (F). The CA-response of 1 mM ACh and other potential interfering molecules of GI (1mM), H_2O_2 (1mM), AA (1mM), DA (0.1mM), Tr (0.1mM), Ad (0.1mM), Gu (0.1mM), AD (0.1mM), and NA (0.1mM) on $\text{Mn}_2\text{O}_3\text{FL/C/GCE}$ (G) and $\text{Mn}_2\text{O}_3\text{FL/C/GCE}$ (H) at $E = 0.6$ V in 0.1 M NaOH electrolyte solution.

Selectivity ACh sensor of $\text{Mn}_2\text{O}_3\text{NLS/C/GCE}$ and $\text{Mn}_2\text{O}_3\text{FL/C/GCE}$ in human fluids

Selectivity is one of the potential and intrinsic factors present in the design of sensors/biosensors. The selectivity of $\text{Mn}_2\text{O}_3\text{NLS/C/GCE}$ and $\text{Mn}_2\text{O}_3\text{FL/C/GCE}$ -based ACh sensors was studied using CA (at 0.6 V) in the presence of other potential interfering molecules. Human fluids contain multiple interfering molecules that may reduce/increase the response to ACh. The potential interfering

molecules in human serum samples include Glucose (GI), dopamine (DA), adrenaline (AD), tryptophan (Tr), AA, H₂O₂, adenine (Ad), guanine (Gu), and noradrenaline (NA). Figure 4G displays the CA-response after the addition of 1 mM ACh, other interfering molecules, and then 1 mM ACh was added. The Mn₂O₃FL/C/GCE sensor activity showed an increased current response upon ACh addition before and after the inclusion of interfering molecules. This behavior illustrates the successful assembling of a highly selective electrode for ACh recognition in the presence of other interfering molecules. Similarly, selectivity studies were performed by CA on Mn₂O₃NLs/C/GCE with the addition of ACh molecules and other interfering molecules. The Mn₂O₃NLs/C/GCE showed a selective nonenzymatic sensor design for detecting ACh molecules in the presence of potential interfering molecules. These results are due to the nanoengineered structures of Mn₂O₃ and the active doping of these materials by carbon-based material.

An actual monitoring assay of ACh was performed using Mn₂O₃FL/C/GCE as a nonenzymatic sensor. The blood serum was purchased from Sigma-Aldrich Company for investigating the ACh molecules in the human fluids. Using the standard addition method, known concentrations of ACh were examined using CA-technique. A sensitive and selective assay of ChA on Mn₂O₃FL/C/GCE has been observed from the fast and strong CA signal of 1 mM ACh in an electrolyte solution containing human serum. The addition of different ACh concentrations with strong and stable CA-signal introduced a highly ACh sensor assay based on Mn₂O₃FL/C/GCE. Figure 5B shows the column plot of various [ACh]/(mM) concentrations Vs. the I_a(μA) values, leading to the design of sensitive and selective nonenzymatic sensors for monitoring ACh in humans' serum samples with % relative standard deviation (RSD) = 3.34%. Thus, the Mn₂O₃FL/C/GCE can be used for analyzing and investigating some neuronal disorders. Scheme 2 shows the ACh-molecules synthesis process in the postsynaptic cells. The ACh-molecules are regarded as one of the neurotransmitters in the nervous system. Through the nonenzymatic ACh electrooxidation, the surface of Mn₂O₃FL/C/GCE acted as the mimetic catalase like acetylcholine esterase. The ACh-molecules were hydrolyzed into choline and acetic acid and then electrochemically oxidized with the generation of electrons and formation of betaine molecules in fast time and high efficiency. Therefore, the Mn₂O₃ structures of nanolayers and flower-like structures decorated by C propounded a functionalized electrode surface for selective monitoring of ACh in biological fluids.



Scheme 2. The schematic synthesis and detection of acetylcholine (ACh) on Mn₂O₃FL/C. A) The synthesis of acetylcholine (ACh) in the postsynaptic cells. B) The diffusion of the ACh at the surface of Mn₂O₃FL/C and electrochemical signaling of ACh with loss of 2e⁻.

ACh nonenzymatic sensor stability and reproducibility based on Mn₂O₃NLs/C/GCE and Mn₂O₃FL/C/GCE

Stability and reproducibility are regarded as key factors for producing an economical and commercial sensor assay. In this regard, the reproducibility and stability of Mn₂O₃NLs/C/GCE and Mn₂O₃FL/C/GCE were studied by multiple measurements of ACh concentrations using various electrodes. Figures 5C and 5E show the column plot of electrode numbers (n = 10) versus the I_a (μA) values to 0.1 mM ACh for Mn₂O₃FL/C/GCE and Mn₂O₃NLs/C/GCE, respectively. These data show the high reproducibility of the designed electrodes, which can be redesigned with high efficiency with an RSD of 0.93%. The 0.2 mM ACh was measured 10 times by CA using the same electrode of Mn₂O₃FL/C/GCE and Mn₂O₃NLs/C/GCE and washed by DI H₂O after each measurement. Stable nonenzymatic ACh sensors were designed based on Mn₂O₃FL/C/GCE and Mn₂O₃NLs/C/GCE. The column plots of the sample numbers versus CA current values illustrate the stable measurement of ACh after further use. The electrode sensitivity loss was 1% from the first measurement with %RSD of 1.01% and 0.84% (Figures 5D and 5F, respectively). Therefore, the designed nonenzymatic sensors based on Mn₂O₃FL/C/GCE and Mn₂O₃NLs/C/GCE showed highly stable and reproducible sensors for detecting ACh molecules^{33, 75, 76}.

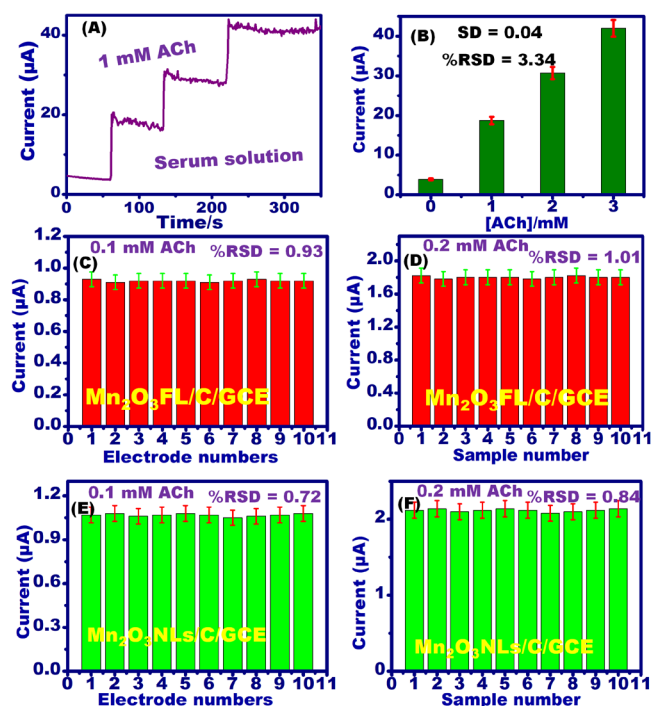


Figure 5. The CA response of 1 mM ACh added into the human serum solution (100 μ L blood serum to 9.9 mL 0.1 M NaOH) on $\text{Mn}_2\text{O}_3\text{FL/C/GCE}$ at $E = 0.6$ V. The column plot of electrode number versus the $I_a/\mu\text{A}$ for measuring of 0.1 mM ACh on $\text{Mn}_2\text{O}_3\text{FL/C/GCE}$ (C) and $\text{Mn}_2\text{O}_3\text{NLS/C/GCE}$ (E). The column plot of sample number Vs the $I_a/\mu\text{A}$ for measuring 0.2 mM ACh on $\text{Mn}_2\text{O}_3\text{FL/C/GCE}$ (D) and $\text{Mn}_2\text{O}_3\text{NLS/C/GCE}$ (F).

Conclusions

Hybrid Mn_2O_3 nanostructured materials decorated by C ($\text{Mn}_2\text{O}_3\text{NLS/C}$ and $\text{Mn}_2\text{O}_3\text{FL/C}$) were designed as active materials for ACh molecules monitoring in human fluids. The cracked NLS structure enlarged the contact area between the electrolyte and the electrode surface. Moreover, the features of FL structure of $\text{Mn}_2\text{O}_3\text{FL/C}$ led to the creation of a highly active interfacial surface with high loading/diffusion of the target through the inner/outer electrode surface. The presence of C on the surface of Mn_2O_3 created a multi-functional active site, sustained the electrochemical activity, and enhanced the material stability toward ACh electrooxidation on Mn_2O_3 active sites. In addition, the sensitivity and stability of Mn_2O_3 for the detection of ACh at high concentrations were enhanced. The designed ACh sensors based on $\text{Mn}_2\text{O}_3\text{NLS/C}$ and $\text{Mn}_2\text{O}_3\text{FL/C}$ produced highly sensitive nonenzymatic sensors with low LOD of 2 ± 0.002 and 7 ± 0.001 μM and a wide linear range of 0.1–7 mM with fast response (>5 s), respectively. The designed sensors provided high stability and good reproducibility after multiple uses with a %RSD of 0.5%–1.4%. The designed nonenzymatic sensors of $\text{Mn}_2\text{O}_3\text{NLS/C}$ and $\text{Mn}_2\text{O}_3\text{FL/C}$ detected ACh in human fluids with high recovery, sensitive and stable signal, and fast response. Therefore, the nonenzymatic ACh sensors based on $\text{Mn}_2\text{O}_3\text{NLS/C}$ and $\text{Mn}_2\text{O}_3\text{FL/C}$ can be employed

in ACh sensor assays and used for the follow-up investigation of several neuronal disorders.

Conflicts of interest

There are no conflicts to declare

Acknowledgements

This work was supported by the Japan Society for the Promotion of Science (JSPS), grant No. P19067.

Notes and references

- J. Cai, F. Hua, L. Yuan, W. Tang, J. Lu, S. Yu, X. Wang and Y. Hu, *BioMed Res. Int.*, 2014, **2014**.
- A. Eliassen, K. P. Dalhoff and H. Horwitz, *J. Neurology*, 2018, **265**, 1303-1309.
- B. R. Bloem, E. R. Dorsey and M. S. Okun, *JAMA neurology*, 2020, **77**, 927-928.
- B. R. Bloem, E. J. Henderson, E. R. Dorsey, M. S. Okun, N. Okubadejo, P. Chan, J. Andrejack, S. K. L. Darweesh and M. Munneke, *The Lancet Neurology*, 2020, **19**, 623-634.
- D. A. Brown, *British J. Pharmacol.*, 2006, **147**, S120-S126.
- M. R. Picciotto, M. J. Higley and Y. S. Mineur, *Neuron*, 2012, **76**, 116-129.
- M. L. Colombo, J. V. Sweedler and M. Shen, *Anal. Chem.*, 2015, **87**, 5095-5100.
- S. Upadhyay, G. R. Rao, M. K. Sharma, B. K. Bhattacharya, V. K. Rao and R. Vijayaraghavan, *Biosens. Bioelectron.*, 2009, **25**, 832-838.
- J. D. Keighron, J. Wigström, M. E. Kurczyk, J. Bergman, Y. Wang and A.-S. Cans, *ACS Chem. Neurosc.*, 2015, **6**, 181-188.
- S. Liao, Y. Qiao, W. Han, Z. Xie, Z. Wu, G. Shen and R. Yu, *Anal. Chem.*, 2012, **84**, 45-49.
- C. Zhang, Y. Fan, H. Zhang, S. Chen and R. Yuan, *Anal. Bioanal. Chem.*, 2019, **411**, 905-913.
- C. Ye, M.-Q. Wang, X. Zhong, S. Chen, Y. Chai and R. Yuan, *Biosens. Bioelectron.*, 2016, **79**, 34-40.
- Y. Chen, S. Zhou, L. Li and J.-j. Zhu, *Nano Today*, 2017, **12**, 98-115.
- L. Montali, M. M. Calabretta, A. Lopreside, M. D'Elia, M. Guardigli and E. Michelini, *Biosens. Bioelectron.*, 2020, **162**, 112232.
- J. Qian, X. Yang, L. Jiang, C. Zhu, H. Mao and K. Wang, *Sens. Actuators B: Chem.* 2014, **201**, 160-166.
- C.-I. Wang, A. P. Periasamy and H.-T. Chang, *Anal. Chem.*, 2013, **85**, 3263-3270.
- P. Song, N. D. Hershey, O. S. Mabrouk, T. R. Slaney and R. T. Kennedy, *Anal. Chem.*, 2012, **84**, 4659-4664.
- G. E. Fenoy, W. A. Marmisollé, O. Azzaroni and W. Knoll, *Biosens. Bioelectron.*, 2020, **148**, 111796.
- P. Balasubramanian, T. S. T. Balamurugan, S.-M. Chen and T.-W. Chen, *ACS Sustain. Chem. Eng.* 2019, **7**, 7642-7651.
- S. Z. Mohammadi, H. Beitollahi and S. Tajik, *Micro and Nano Sys. Lett.*, 2018, **6**, 1-7.

21. M. Y. Emran, S. A. El-Safty, M. M. Selim and M. A. Shenashen, *Sens. Actuators B: Chem.*, 2021, **329**, 129192.
22. M. Y. Emran, M. A. Shenashen, S. A. El-Safty, M. M. Selim, T. Minowa and A. Elmarakbi, *ACS Appl. Bio Mater.*, 2020, **3**, 8496-8506.
23. M. Y. Emran, S. A. El-Safty, M. M. Selim, T. Minowa, A. Elmarakbi and M. A. Shenashen, *Anal. Chim. Acta*, 2021, **1142**, 143-156.
24. M. Y. Emran, S. A. El-Safty, M. M. Selim, A. Reda, H. Morita and M. A. Shenashen, *Carbon*, 2021, **173**, 1093-1104.
25. N. Chauhan, S. Balayan and U. Jain, *Synth. Metals*, 2020, **263**, 116354.
26. H. S. Magar, M. E. Ghica, M. N. Abbas and C. M. A. Brett, *Talanta*, 2017, **167**, 462-469.
27. M. Y. Emran, H. Khalifa, H. Goma, M. A. Shenashen, N. Akhtar, M. Mekawy, A. Faheem and S. A. El-Safty, *Microchim. Acta*, 2017, **184**, 4553-4562.
28. M. Y. Emran, M. Mekawy, N. Akhtar, M. A. Shenashen, I. M. El-Sewify, A. Faheem and S. A. El-Safty, *Biosens. Bioelectron.*, 2018, **100**, 122-131.
29. H. Khalifa, S. A. El-Safty, A. Reda, M. M. Selim and M. A. Shenashen, *Energy Storage Mater.*, 2021, **37**, 363-377.
30. H. Khalifa, S. El-Safty, A. Reda, A. Elmarakbi, H. Metawa and M. Shenashen, *Appl. Mater. Today*, 2020, **19**, 100590.
31. H. Khalifa, S. A. El-Safty, A. Reda, M. A. Shenashen and A. I. Eid, *Nat. Sci. Rev.*, 2020, **7**, 863-880.
32. B. Li, P. Gu, Y. Feng, G. Zhang, K. Huang, H. Xue, H. Pan, *Adv. Funct. Mater.*, 2017, **27**, 1605784.
33. M. Y. Emran, M. A. Shenashen, A. A. Abdelwahab, M. Abdelmottaleb, M. Khairy and S. A. El-Safty, *Electrocatalysis*, 2018, **9**, 514-525.
34. M. He, L. Cao, W. Li, X. Chang and Z. Ren, *J. Alloys and Compounds*, 2021, **865**, 158934.
35. N. Sohal, B. Maity, S. Basu, *ACS Appl. Nano Mater.* 2020, **3**, 5955-5964.
36. N. Sohal, B. Maity, S. Basu, *ACS Appl. Bio Mater.* 2021, **4**, 5158-5168.
37. X. Yan, Y. Song, X. Wu, C. Zhu, X. Su, D. Du and Y. Lin, *Nanoscale*, 2017, **9**, 2317-2323.
38. M. Anantha, S. K. Kumar, D. Anarghya, K. Venkatesh, M. Santosh, K. Y. Kumar and H. Muralidhara, *Sensors Int.*, 2021, **2**, 100087.
39. C. Zhang, X. Yu, H. Chen, L. Li, D. Sun, X. Chen and X. Hao, *J. Alloys and Compounds*, 2021, **864**, 158685.
40. C. Guo, H. Li, X. Zhang, H. Huo and C. Xu, *Sens. Actuators B: Chem.*, 2015, **206**, 407-414.
41. H. J. Won, A. I. Robby, H. S. Jhon, I. In, J. H. Ryu and S. Y. Park, *Sens. Actuators B: Chem.*, 2020, **320**, 128391.
42. S. D. Jereil, K. Vijayalakshmi and A. Monamary, *Ceramics Int.*, 2018, **44**, 8064-8071.
43. K. Vijayalakshmi, S. D. Jereil and K. Alagusundaram, *Ceramics Int.*, 2017, **43**, 14464-14472.
44. K. Vijayalakshmi, A. Renitta, K. Alagusundaram and A. Monamary, *Mater. Chem. Phys.*, 2018, **214**, 431-439.
45. Y. Shu, J. Xu, J. Chen, Q. Xu, X. Xiao, D. Jin, H. Pang and X. Hu, *Sens. Actuators B: Chem.*, 2017, **252**, 72-78.
46. S.-J. Li, J.-C. Zhang, J. Li, H.-Y. Yang, J.-J. Meng and B. Zhang, *Sens. Actuators B: Chem.*, 2018, **260**, 1-11.
47. W. Wang, J. Liu, Q. Zhang, X. Zhou and B. Liu, *Food Control*, 2019, **105**, 29-37.
48. J. Qian, Z. Yang, C. Wang, K. Wang, Q. Liu, D. Jiang, Y. Yan and K. Wang, *J. Mater. Chem. A*, 2015, **3**, 13671-13678.
49. N. Akhtar, M. Y. Emran, M. A. Shenashen, H. Khalifa, T. Osaka, A. Faheem, T. Homma, H. Kawarada and S. A. El-Safty, *J. Mater. Chem. B*, 2017, **5**, 7985-7996.
50. D.-G. Lee, H. Jeong, K.-W. Jeon, L. Zhang, K. Park, S. Ryu, J. Kim and I. S. Lee, *J. Mater. Chem. A*, 2017, **5**, 22341-22351.
51. P. Pal, A. K. Giri, S. Mahanty and A. B. Panda, *CrystEngComm*, 2014, **16**, 10560-10568.
52. R. Naeem, R. Yahya and M. Mazhar, *Dalton Trans.* 2016, **45**, 14928-14939.
53. N. Sohal, B. Maity, N. P. Shetti, S. Basu, *ACS Appl. Nano Mater.* 2021, **4**, 2285-2302.
54. H. Rahaman, R. M. Laha, D. K. Maiti and S. K. Ghosh, *RSC Adv.*, 2015, **5**, 33923-33929.
55. Y. Park, S. W. Lee, K. H. Kim, B.-K. Min, A. K. Nayak, D. Pradhan and Y. Sohn, *Sci. Rep.*, 2015, **5**, 1-11.
56. Z. Geng, Y. Wang, J. Liu, G. Li, L. Li, K. Huang, L. Yuan and S. Feng, *ACS Appl. Mater. Interfaces*, 2016, **8**, 27825-27831.
57. N. Akhtar, S. A. El-Safty, M. E. Abdelsalam, M. A. Shenashen and H. Kawarada, *Biosens. Bioelectron.*, 2016, **77**, 656-665.
58. W. Li, X. Guo, P. Geng, M. Du, Q. Jing, X. Chen, G. Zhang, H. Li, Q. Xu, P. Braunstein, H. Pang, *Adv. Mater.*, 2021, **33**, 2105163.
59. D. Buttry and A. Bard, *Electroanalytical chemistry*, 1991, **17**.
60. K. Ahmad and S. M. Mobin, *Nanoscale Adv.*, 2019, **1**, 719-727.
61. M. Y. Emran, M. A. Shenashen, A. A. Abdelwahab, M. Abdelmottaleb and S. A. El-Safty, *New J. Chem.*, 2018, **42**, 5037-5044.
62. T. N. Kulikova, A. V. Porfireva, G. A. Evtugyn and T. Hianik, *Electroanalysis*, 2019, **31**, 1913-1924.
63. M. Y. Emran, M. A. Shenashen, H. Morita and S. A. El-Safty, *Adv. Healthcare Mater.*, 2018, **7**, 1701459.
64. H. Khalifa, M.A. Shenashen, A. Reda, M.M. Selim, A. Elmarakbi, S.A. El-Safty, *Nano-Micro Lett.* 2019, **11**, 84.
65. M.Y. Emran, M.A. Shenashen, S.A. El-Safty, M. M. Selim, *Microp. Mesop. Mater.* 2021, **320**, 111097.
66. P. Balasubramanian, T. Balamurugan, S.-M. Chen, T.-W. Chen and T. Sathesh, *ACS Sust. Chem. Eng.*, 2018, **7**, 5669-5680.
67. R. Ponnusamy, R. Venkatesan, M. Kandasamy, B. Chakraborty and C. S. Rout, *Appl. Surface Sci.*, 2019, **487**, 1033-1042.
68. J. Chen, W.-D. Zhang and J.-S. Ye, *Electrochem. Commun.*, 2008, **10**, 1268-1271.
69. L. Wang, X. Chen, C. Liu and W. Yang, *Sens. Actuators B: Chem.*, 2016, **233**, 199-205.
70. M. Y. Emran, S. A. El-Safty, M. A. Shenashen and T. Minowa, *Sens. Actuators B: Chem.*, 2019, **284**, 456-467.
71. A. A. Abdelwahab, A. H. Naggat, M. Abdelmottaleb and M. Y. Emran, *Electroanalysis*, 2020, **32**, 2156-2165.
72. X. Li, J. Wei, Q. Li, S. Zheng, Y. Xu, P. Du, C. Chen, J. Zhao, H. Xue, Q. Xu, H. Pang, *Adv. Funct. Mater.*, 2018, **28**, 1800886.

73. A. Singh, A. Chandra, *Sci. Rep.* 2015, 5, 15551.

74. M. Hadadian, J.-H. Smått, J.-P. Correa-Baena, *Energy Environ. Sci.*, 2020, 13, 1377-1407

75. X. Li, M. A. Shenashen, X. Wang, A. Ito, A. Taniguchi and S. A. El-Safty, *Adv. Biosys.*, 2018, 2, 1700114.

76. X. Li, M. A. Shenashen, X. Wang, A. Ito, A. Taniguchi and S. A. El-Safty, *Sci. Rep.*, 2017, 7, 16749.